Geophys. J. Int. (2002) **148,** 389–401

A finite-element algorithm for electromagnetic induction in two-dimensional anisotropic conductivity structures

Yuguo Li*

Geophysikalisches Institut der Universität Göttingen, Postfach 2341, D-37013 *Göttingen, Germany*

Accepted 2001 July 31. Received 2001 July 30; in original form 2000 February 18

SUMMARY

Electromagnetic fields are computed for a 2-D electrically anisotropic earth using a finite-element technique. The models consist of a background layered structure, containing anisotropic blocks. Each block and layer may be anisotropic by assigning to them 3×3 conductivity tensors. The forward modelling problem leads to a coupled system of two partial differential equations for the strike-parallel field components E_x and H_x. They are solved numerically using the finite-element (FE) method. The resulting system of linear FE equations is solved using a preconditioned conjugate gradient method. Subsequently, strike-perpendicular field components E_y and H_y at the surface are found by numerical differentiation of E_x and H_x, using spline interpolation.

The 2-D FE algorithm has been validated by comparison with a 2-D finite-difference solution. Three model types are used to demonstrate the effect of anisotropy upon the magnetotelluric responses: horizontal, vertical and dipping anisotropy. A fourth model simulates the effect of anisotropy in the context of shear and subduction zones. The model responses simulate the splitting of apparent resistivity curves at long periods, as well as the existence of tensor impedances with significant diagonal elements, as has been observed previously.

Key words: electrical anisotropy, electromagnetic induction, finite-element method, magnetotellurics, 2-D conductivity structures.

1 INTRODUCTION

In recent years, increased attention has been paid in electromagnetic induction studies to the influence of electrical anisotropy, notably in attempts to fully understand magnetotelluric (MT) observations at longer periods. The magnetotelluric measurements from the Canadian shield reveal pronounced electrical anisotropy in the lower crust and upper mantle (Kellett *et al.* 1992; Mareschal *et al.* 1995). The large anisotropy of MT curves from around the German Deep Drilling site (KTB) is interpreted using an electrically highly anisotropic upper to middle crust (Eisel & Haak 1999). Rasmussen (1988) suggested an anisotropic model within a deep crust layer to explain MT data along a transect in southern Sweden. The effect of anisotropy for a layered structure was initially studied by O'Brien & Morrison (1967). Investigations of 2-D anisotropic models began with the work of Reddy & Rankin (1975), who considered just the effect of horizontal anisotropy. More recently, Osella & Martinelli (1993) calculated the magnetotelluric response of models with smooth irregular boundaries and with a special orientation of principal axes. Schmucker (1994) presented an algorithm for the computation of the electromagnetic induction in a non-uniform thin sheet above a layered half-space, which may contain one or more layers of anisotropic conductivity. Using the finite-difference (FD) method, Pek & Verner (1997) and Weidelt (1996) modelled the MT response of generally anisotropic 2-D and 3-D structures, respectively, with arbitrary orientation of the principal axes.

In this paper, 2-D anisotropic structures are again studied, but now using the finite-element (FE) technique. First, we describe the numerical realization of the FE algorithm in detail. Then, we demonstrate the application of the algorithm by simulating the MT response for various simple test models. Our results are compared with the finite-difference solution of Pek & Verner (1997). Finally, we calculate the MT response of three types of anisotropy: horizontal, vertical and dipping anisotropy. We conclude with a model that simulates the tectonic setting of a geological shearzone or a downgoing slab in a subduction zone. The main aim of this contribution is to present a FE scheme for electromagnetic induction in 2-D anisotropic structures. Though the FD solution for this problem is available, the FE solution is needed because both the FD and FE methods have their own particular advantages and serve as cross-check for each other. In addition, the FE method can handle the non-rectilinear geometry needed for modelling of realistic earth structures.

* Now at: Institute of Geophysics, Freiberg University of Mining and Technology, 09596 Freiberg, Germany.

© 2002 RAS

2 BOUNDARY VALUE PROBLEM

Consider the 2-D model shown in Fig. 1. The shaded anomalous region is embedded into a single layer within the normal structure, which consists of n layers and its bottom layer extends downward to infinity. For simplicity, the anomalous region is shown without internal boundaries as a single block of directional-dependent conductivity $\underline{\underline{\sigma}}$ which differs in at least one element from the surrounding conductivity tensor $\underline{\underline{\sigma}}_j$ in the jth layer. Our program allows, however, for more general model structures, with subdivided anomalous regions into various uniform blocks and with contacts to more than one layer.

The anomalous region can extend in the positive y-direction to infinity, i.e. the model may merge here into a new layered normal structure. At this state the algorithm excludes induction by sources with a significant lateral non-uniformity within the lateral range of the numerical solution. The model is invariant in the strike direction x. The inducing electromagnetic field is also invariant in the x-direction, even though field vectors will have three components for polarizations of the magnetic source parallel or perpendicular to the strike, owing to the anisotropy. Hence, the usual distinction between TE and TM modes for 2-D isotropic structures becomes invalid. This has the consequence that, when the primary magnetic vector is perpendicular to the strike, the electric field will have components in the direction of the primary field, leading to a charge build up on boundaries (except for the special case of dipping anisotropy).

Assuming a time variation $e^{-i\omega t}$, the governing equations for the electromagnetic field in the quasi-stationary approximation are

$$\nabla\times\mathbf{E}=i\omega\mu_0\mathbf{H}, \qquad \nabla\times\mathbf{H}=\underline{\sigma}\mathbf{E}, \tag{1}$$

where μ_0 is the magnetic permeability of free space, and

$$\underline{\sigma}=\begin{pmatrix}\sigma_{xx} & \sigma_{xy} & \sigma_{xz}\\ \sigma_{yx} & \sigma_{yy} & \sigma_{yz}\\ \sigma_{zx} & \sigma_{zy} & \sigma_{zz}\end{pmatrix}$$

is the electric conductivity tensor. The tensor is symmetric, and when rotated into the direction of its principal axes (x', y', z'), it is given by

$$\underline{\sigma'}=\begin{pmatrix}\sigma_{x'} & 0 & 0\\ 0 & \sigma_{y'} & 0\\ 0 & 0 & \sigma_{z'}\end{pmatrix}.$$

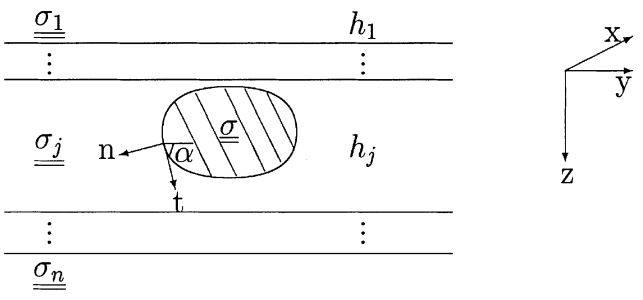

Figure 1. The 2-D anisotropic model considered in this paper.

In the special 2-D case, eq. (1) reduces for a homogeneous block of constant conductivity to

$$\frac{\partial E_z}{\partial y}-\frac{\partial E_y}{\partial z}=i\omega\mu_0 H_x, \tag{2}$$

$$\frac{\partial E_x}{\partial z}=i\omega\mu_0 H_y, \tag{3}$$

$$-\frac{\partial E_x}{\partial y}=i\omega\mu_0 H_z; \tag{4}$$

$$\frac{\partial H_z}{\partial y}-\frac{\partial H_y}{\partial z}=\sigma_{xx}E_x+\sigma_{xy}E_y+\sigma_{xz}E_z, \tag{5}$$

$$\frac{\partial H_x}{\partial z}=\sigma_{yx}E_x+\sigma_{yy}E_y+\sigma_{yz}E_z, \tag{6}$$

$$-\frac{\partial H_x}{\partial y}=\sigma_{zx}E_x+\sigma_{zy}E_y+\sigma_{zz}E_z. \tag{7}$$

It is now evident that if the strike-parallel components E_x and H_x have been found, the remaining components E_y, E_z, H_y and H_z can be obtained from spatial derivatives of E_x and H_x. Eqs (2)–(7) can be combined to yield two second-order differential equations for the strike-parallel components E_x and H_x:

$$\frac{1}{i\omega\mu_0}\nabla^2E_x+CE_x+A\frac{\partial H_x}{\partial y}-B\frac{\partial H_x}{\partial z}=0, \tag{8}$$

$$\nabla\cdot(\underline{\tau}\nabla H_x)+i\omega\mu_0H_x-\frac{\partial(AE_x)}{\partial y}+\frac{\partial(BE_x)}{\partial z}=0, \tag{9}$$

where

$$D=\sigma_{yy}\sigma_{zz}-\sigma_{yz}\sigma_{zy}, \qquad A=(\sigma_{yx}\sigma_{zy}-\sigma_{zx}\sigma_{yy})/D,$$

$$B=(\sigma_{zx}\sigma_{yz}-\sigma_{yx}\sigma_{zz})/D, \quad C=\sigma_{xx}+\sigma_{xy}B+\sigma_{xz}A,$$

$$\underline{\tau}=\frac{1}{D}\begin{pmatrix}\sigma_{yy} & \sigma_{yz}\\ \sigma_{zy} & \sigma_{zz}\end{pmatrix}.$$

From eqs (8) and (9) it is clear that anisotropy couples the otherwise independent strike-parallel components E_x and H_x through first-order partial derivatives. Consequently, there are no separate TE and TM modes for the anomalous field in the general anisotropic case. Hence, these equations must be solved simultaneously for E_x and H_x.

In the forthcoming presentation of modelling results, various special forms of anisotropy will be considered. Assuming as in Fig. 1 a uniform anomalous domain and isotropy for the surrounding normal structure, one or two of the principal axes of $\underline{\sigma}$ are taken to be parallel to corresponding axes of (x, y, z) coordinates.

2.1 Horizontal anisotropy

With $\sigma_{xz}=\sigma_{yz}=0$, the principal axis z' is vertical, the remaining two principal axes x' and y' are in the horizontal plane (x, y) with strike angle α with respect to the x axis. Eqs (8) and (9)

then reduce to

$$\frac{1}{i\omega\mu_0}\nabla^2 E_x + \left(\sigma_{xx} - \frac{\sigma_{xy}^2}{\sigma_{yy}}\right)E_x + \frac{\sigma_{xy}}{\sigma_{yy}}\frac{\partial H_x}{\partial z} = 0\,, \tag{10}$$

$$\frac{\partial}{\partial y}\left(\frac{1}{\sigma_{zz}}\frac{\partial H_x}{\partial y}\right) + \frac{\partial}{\partial z}\left(\frac{1}{\sigma_{yy}}\frac{\partial H_x}{\partial z}\right) + i\omega\mu_0 H_x - \frac{\partial}{\partial z}\left(\frac{\sigma_{xy}}{\sigma_{yy}}E_x\right) = 0\,. \tag{11}$$

The induction equations become simpler than eqs (8) and (9), but the strike-parallel components E_x and H_x are still coupled through first-order partial derivatives with respect to z. So eqs (10) and (11) must be solved jointly in order to obtain E_x and H_x.

2.2 Dipping anisotropy

With $\sigma_{xy}=\sigma_{xz}=0$, the principal axis x' of the conductivity tensor is horizontal and in the strike direction, the remaining two principal axes y' and z' are in the vertical plane (y, z) with dip angle β with respect to the y axis. Now eqs (8) and (9) decouple into two independent modes

$$\nabla^2 E_x + i\omega\mu_0\sigma_{xx}E_x = 0\,, \tag{12}$$

$$\nabla\cdot(\underline{\underline{\tau}}\nabla H_x) + i\omega\mu_0 H_x = 0\,. \tag{13}$$

Eq. (12) for E-polarization can be solved using algorithms for 2-D isotropic structures—only the electric conductivity has to be replaced by σ_{xx} as scalar conductivity. However, the resulting expression for the TM mode is still complicated.

2.3 Vertical anisotropy

If $\sigma_{xy}=\sigma_{xz}=\sigma_{yz}=0$, all three principal axes of the conductivity tensor are coincident with the axes of the (x, y, z) coordinates. If in addition $\sigma_{xx}=\sigma_{yy}=\sigma_h$, this results in an axially symmetric situation with respect to z, in which the conductivity σ_h for any horizontal direction differs solely from $\sigma_{zz}=\sigma_v$ in the vertical direction. This again decouples eqs (8) and (9), and we have

$$\nabla^2 E_x + i\omega\mu_0\sigma_{\rm h}E_x = 0\,, \tag{14}$$

$$\frac{\partial}{\partial y}\left(\frac{1}{\sigma_v}\frac{\partial H_x}{\partial y}\right) + \frac{\partial}{\partial z}\left(\frac{1}{\sigma_{\rm h}}\frac{\partial H_x}{\partial z}\right) + i\omega\mu_0 H_x = 0\,. \tag{15}$$

Though the induction equation for B-polarization becomes much simpler than eq. (9), it cannot be solved by using 2-D isotropic algorithms, because the conductivities in the horizontal and vertical directions are different. If they are the same, then eq. (15) also reduces to the isotropic case. The following boundary conditions apply: on the outer boundary of the model, Dirichlet boundary conditions are set, constructed from 1-D solutions for the corresponding layered earth at the left- and right-hand side of the model. At the top and the bottom of the model, the boundary conditions are constructed as linear interpolations of the respective 1-D values at the left- and right-hand sides of the model (Pek & Verner 1997). On inner boundaries, the tangential components of both electric and magnetic fields, $E_{\rm t}$ and $H_{\rm t}$, must be continuous. From Fig. 1, $E_{\rm t}$ and $H_{\rm t}$ are

$$E_{\rm t} = E_y\cos\alpha + E_z\sin\alpha\,,$$

$$H_{\rm t} = H_y\cos\alpha + H_z\sin\alpha\,.$$

It is now essential, to reformulate these relations as follows. Let $\mathbf{n}$ be the outward normal unit vector to the inhomogeneous region, and

$$\mathbf{p} = -AE_x\mathbf{e}_y + BE_x\mathbf{e}_z\,, \tag{16}$$

with A and B from eqs (8) and (9), with $\mathbf{e}_y$ and $\mathbf{e}_z$ being the unit vectors along the y- and z-axes, respectively. Then, after substantial derivations, the expressions

$$E_{\rm t} = \underline{\underline{\tau}}\frac{\partial H_x}{\partial n} + \mathbf{p}\cdot\mathbf{n} \tag{17}$$

and

$$H_{\rm t} = \frac{1}{i\omega\mu_0}\frac{\partial E_x}{\partial n} \tag{18}$$

are found for the tangential field components. The formulation of eq. (17) is by no means self-evident and is essential for the following derivations. Only with these expressions do the basic integro-differential eqs (23) and (24) obtain their highly condensed form, which conditions them for a straightforward numerical treatment. More details are described in Li (2000).

3 FINITE-ELEMENT METHOD

The numerical approximation of the problem, posed by eqs (8) and (9), will be based on the finite-element approach. The strike-parallel field components, E_x and H_x, are tangential to the conductivity structures and thus continuous everywhere. Hence the assumption made in finite-element modelling that all the field components are continuous across element boundaries is satisfied. The approximation is performed on a model area Ω that entirely embraces the zone of the 2-D inhomogeneities, and extends far enough in all directions for the anomalous fields to be very small on its external boundary. To avoid the singularity of (9) owing to vanishing conductivity within the insulating air layer above the earth, we assume that the air has a very small, but non-zero conductivity, typically less than 10^{-12} Sm^{-1} in our computations. Numerical tests show no substantial dependence of the field solution on air conductivities chosen within broad limits down to 10^{-30} Sm^{-1}.

The method of weighted residuals is used to derive the integral equations from the differential eqs (8) and (9). Eq. (8) is multiplied by an arbitrary variation of the electric field δE_x and integrated over the model area Ω:

$$\int_\Omega\left(\frac{1}{i\omega\mu_0}\nabla^2 E_x + CE_x + A\frac{\partial H_x}{\partial y} - B\frac{\partial H_x}{\partial z}\right)\delta E_x\,d\Omega = 0\,. \tag{19}$$

In this equation, the first term of the integrand contains second-order partial derivatives, and can be simplified by using Green's formula,

$$\int_\Omega \nabla^2 u\,v\,d\Omega = \int_\Gamma \frac{\partial u}{\partial n}\,v\,d\Gamma - \int_\Omega \nabla u\cdot\nabla v\,d\Omega\,,$$

where Γ denotes the boundary of the model area Ω. Then eq. (19) can be written in the equivalent form,

$$\frac{1}{i\omega\mu_0}\int_\Omega \nabla E_x\cdot\nabla\delta E_x\,d\Omega - \int_\Omega CE_x\,\delta E_x\,d\Omega - \int_\Omega A\frac{\partial H_x}{\partial y}\,\delta E_x\,d\Omega + \int_\Omega B\frac{\partial H_x}{\partial z}\,\delta E_x\,d\Omega - \frac{1}{i\omega\mu_0}\int_\Gamma \frac{\partial E_x}{\partial n}\,\delta E_x\,d\Gamma = 0\,. \tag{20}$$

Similarly, eq. (9) is multiplied by an arbitrary variation of the magnetic component δH_x and integrated over the region Ω,

and, subsequently, modified using the Gauss formula

$$\int_\Omega \nabla\cdot\mathbf{u}\, v\, d\Omega = \int_\Gamma \mathbf{u}\cdot\mathbf{n}\, v\, d\Gamma - \int_\Omega \mathbf{u}\cdot\nabla v\, d\Omega .$$

With the use of eq. (16) this leads to the integral equation

$$\int_\Omega \nabla\delta H_x\cdot(\underline{\underline{\tau}}\nabla H_x)\, d\Omega - \int_\Omega i\omega\mu_0 H_x\,\delta H_x\, d\Omega + \int_\Omega \mathbf{p}\cdot\nabla\delta H_x\, d\Omega$$
$$- \int_\Gamma \left(\underline{\underline{\tau}}\frac{\partial H_x}{\partial n} + \mathbf{p}\cdot\mathbf{n}\right)\delta H_x\, d\Gamma = 0 . \qquad (21)$$

Here we have also used the formula

$$\underline{\underline{\tau}}\nabla H_x\cdot\mathbf{n}\delta H_x = \underline{\underline{\tau}}\frac{\partial H_x}{\partial n}\,\delta H_x . \qquad (22)$$

The model area Ω can be subdivided into rectangular or triangular elements. The formulation for the rectangular elements is described by Li (2000). In the following section, the formulations for the triangular elements are presented. The integrals of eqs (20) and (21) thus decompose into integrals for each element, numbered with index $e=1, 2, \ldots, n_e$,

$$\sum_{e=1}^{n_e}\frac{1}{i\omega\mu_0}\int_e \nabla E_x\cdot\nabla\delta E_x\, d\Omega - \sum_{e=1}^{n_e}\int_e C E_x\,\delta E_x\, d\Omega$$
$$+\sum_{e=1}^{n_e}\int_e \left(-A\frac{\partial H_x}{\partial y} + B\frac{\partial H_x}{\partial z}\right)\delta E_x\, d\Omega$$
$$-\sum_{e=1}^{n_e}\int_{\Gamma_e} H_t\,\delta E_x\, d\Gamma = 0 , \qquad (23)$$

$$\sum_{e=1}^{n_e}\int_e \nabla\delta H_x\cdot(\underline{\underline{\tau}}\nabla H_x)\, d\Omega - \sum_{e=1}^{n_e}\int_e i\omega\mu_0 H_x\,\delta H_x\, d\Omega$$
$$+\sum_{e=1}^{n_e}\int_e \mathbf{p}\cdot\nabla\delta H_x\, d\Omega - \sum_{e=1}^{n_e}\int_{\Gamma_e} E_t\,\delta H_x\, d\Gamma = 0 , \qquad (24)$$

where Γ_e denotes the boundary of the element e. In formulating eq. (23) we have used the eq. (18) to convert the integrand of the line integral into $H_t\delta E_x$. In a similar way, the integrand of the line integral in eq. (24) has been obtained using eq. (17).

Boundary conditions must now be applied. On the inter-element boundaries, the continuity of tangential components of electric and magnetic fields (H_x, E_x) is required. As each boundary is traversed twice in opposite directions during the course of the integration, the sum of line integrals over the internal element boundaries is equal to zero. On the outer boundary, since Dirichlet boundary conditions are set, the variations of electric and magnetic fields δE_x and δH_x are equal to zero. Hence the line integral is also zero. In this way, eqs (23) and (24) finally reduce to

$$\sum_{e=1}^{n_e}\frac{1}{i\omega\mu_0}\int_e \nabla E_x\cdot\nabla\delta E_x\, d\Omega - \sum_{e=1}^{n_e}\int_e C E_x\,\delta E_x\, d\Omega$$
$$+\sum_{e=1}^{n_e}\int_e \left(-A\frac{\partial H_x}{\partial y} + B\frac{\partial H_x}{\partial z}\right)\delta E_x\, d\Omega = 0 , \qquad (25)$$

$$\sum_{e=1}^{n_e}\int_e \nabla\delta H_x\cdot(\underline{\underline{\tau}}\nabla H_x)\, d\Omega - \sum_{e=1}^{n_e}\int_e i\omega\mu_0 H_x\,\delta H_x\, d\Omega$$
$$+\sum_{e=1}^{n_e}\int_e \mathbf{p}\cdot\nabla\delta H_x\, d\Omega = 0 . \qquad (26)$$

Following the basic concept of the FE method in a linear approximation, we assume that in each triangular element the electric field E_x and the magnetic field H_x are linear functions of y and z, and can be approximated by

$$E_x(y, z) = \sum_{i=1}^{3} N_i E_i , \qquad H_x(y, z) = \sum_{i=1}^{3} N_i H_i , \qquad (27)$$

where E_i and H_i are the electric and magnetic fields at the ith vertex with the coordinate (y_i, z_i), $i=1, 2, 3$, of the triangular element Δ_{123} (Fig. 2), and N_i are linear *shape functions*. They are defined by

$$N_i = \frac{1}{2\Delta}(a_i y + b_i z + c_i) , \quad i = 1, 2, 3 , \qquad (28)$$

where

$$\Delta = \frac{1}{2}(a_1 b_2 - a_2 b_1) , \qquad \text{the area of the element } \Delta_{123} , \qquad (29)$$

$$a_1 = z_2 - z_3 , \quad b_1 = y_3 - y_2 , \quad c_1 = y_2 z_3 - y_3 z_2 , \qquad (30)$$

$$a_2 = z_3 - z_1 , \quad b_2 = y_1 - y_3 , \quad c_2 = y_3 z_1 - y_1 z_3 , \qquad (31)$$

$$a_3 = z_1 - z_2 , \quad b_3 = y_2 - y_1 , \quad c_3 = y_1 z_2 - y_2 z_1 . \qquad (32)$$

The area integrals in eqs (25) and (26) over an element are evaluated using eqs (27)–(32). Then the integrals over all elements can be assembled into two linear equation systems. The details are given in Appendix A. Combining these equation systems, we can write the final linear system in the matrix form as

$$\mathbf{K} = \mathbf{0} , \qquad (33)$$

where

$$\mathbf{K} = \begin{pmatrix} \mathbf{K}_{11} & \mathbf{K}_{12} \\ \mathbf{K}_{21} & \mathbf{K}_{22} \end{pmatrix} , \quad \mathbf{U} = \begin{pmatrix} \mathbf{E}_x \\ \mathbf{H}_x \end{pmatrix} .$$

$\mathbf{K}_{11}$ and $\mathbf{K}_{22}$ are symmetric square matrices of order n_d (where n_d is the total number of nodal points in the entire model area Ω), and $\mathbf{K}_{12}$ and $\mathbf{K}_{21}$ are non-symmetric square matrices of

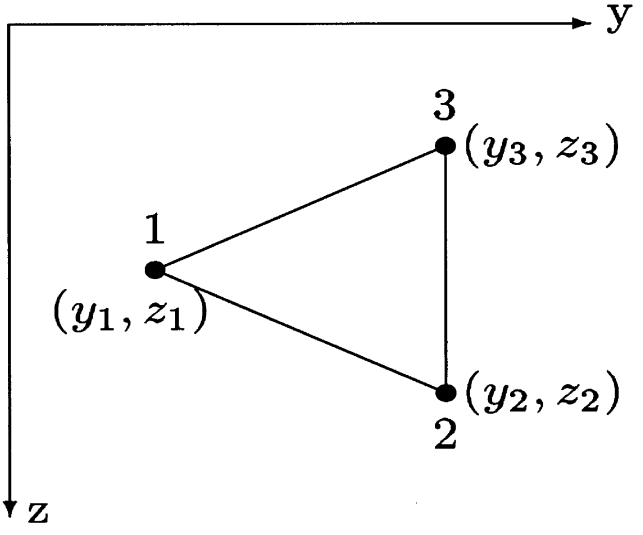

Figure 2. Triangular FE element of the modelled cross-section.

order n_d that satisfy the symmetry relation $\mathbf{K}_{12}=\mathbf{K}_{21}^{\mathrm{T}}$. Hence, the matrix $\mathbf{K}$ is a square symmetric matrix of order $2n_d$. It is sparsely occupied by complex elements. $\mathbf{U}$ is the column vector of order $2n_d$, containing the electric and magnetic fields at all nodal points as unknowns. Substituting the boundary conditions on the outer boundary into eq. (33), these equations can be solved for the field components E_x and H_x at the internal mesh nodes, using the conjugate gradient method.

The conjugate gradient method as originally proposed by Hestens & Stiefel (1952) is only suitable for real symmetric, positive-definite matrices. Jacobs (1981) presented a complex bi-conjugate gradient algorithm that extends the application of the conjugate gradients to complex, indefinite systems. The convergence of this generally conjugate gradient method is improved by preconditioning the coefficient matrix $\mathbf{K}$. We found that a simple diagonal Jacobi scaling (Schwarz 1991) is a sufficient preconditioner in our case. For the models we evaluated in this paper, the grid contains up to 2500 nodes and the number of equation is about 5000. We always used zero values $\mathbf{U}=0$ as starting values, after about 200 iterative steps, we always obtain convergent solutions.

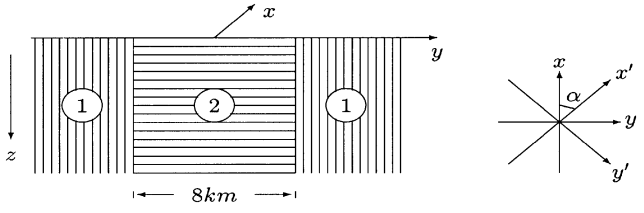

$MEDIUM1:\quad \rho_{x'}=40, \rho_{y'}=100, \rho_{z'}=50, \alpha=55^0$

$MEDIUM2:\quad \rho_{x'}=3\ , \rho_{y'}=10,\ \rho_{z'}=20, \alpha=30^0$

Figure 3. The horizontally anisotropic dyke model of Reddy & Rankin (1975).

In the conjugate gradients method, only the non-zero elements on and below the diagonal of the sparse symmetric coefficient matrix $\mathbf{K}$ are required, which are stored in a 1-D array according to the procedure of Schwarz (1991). With this algorithmic implementation of the conjugate gradient solver, the computer memory requirements of the solution are greatly reduced.

4 MAGNETOTELLURIC IMPEDANCES

Solving the linear equation system eq. (33), we obtain E_x and H_x at each node. The other two magnetic field components H_y, H_z are readily found from eqs (3) and (4), while the relations for the electric components E_y, E_z are derived after some additional calculations from eqs (6) and (7). In summary,

$$H_y=\frac{1}{i\omega\mu_0}\frac{\partial E_x}{\partial z},$$

$$H_z=-\frac{1}{i\omega\mu_0}\frac{\partial E_x}{\partial y},$$

$$E_y=\frac{\sigma_{yz}}{D}\frac{\partial H_x}{\partial y}+\frac{\sigma_{zz}}{D}\frac{\partial H_x}{\partial z}+BE_x,$$

$$E_z=-\frac{\sigma_{yy}}{D}\frac{\partial H_x}{\partial y}-\frac{\sigma_{zy}}{D}\frac{\partial H_x}{\partial z}+AE_x.$$

In our algorithm, the required derivatives are computed numerically using spline interpolation.

The impedance tensor elements can be calculated using the electric and magnetic fields of two orthogonal linear source polarizations, e.g. for the primary magnetic field either in the x-direction with $\mathbf{H}_0=(H_{0x}, H_{0y}, H_{0z})=(-1,0,0)$ (polarization 1) or in the y-direction with $\mathbf{H}_0=(0, 1, 0)$ (polarization 2). The primary field indicates the sum of the inducing field from sources in $z<0$ and of the induced field in the normal structures at

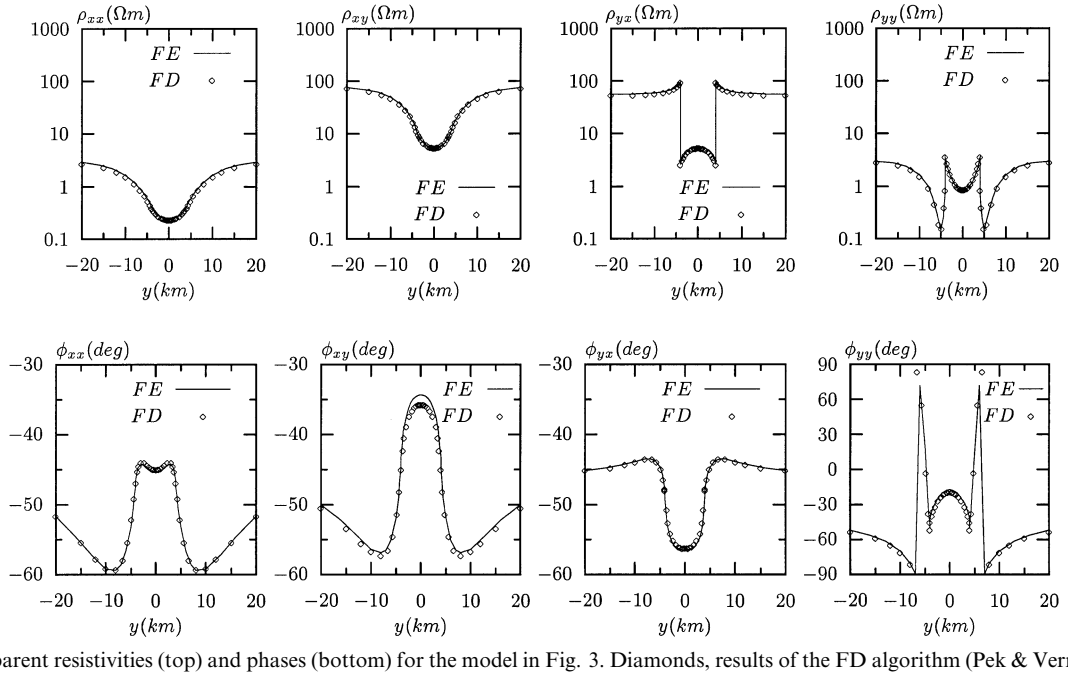

Figure 4. Apparent resistivities (top) and phases (bottom) for the model in Fig. 3. Diamonds, results of the FD algorithm (Pek & Verner 1997); solid line, results of the FE algorithm described in this paper.

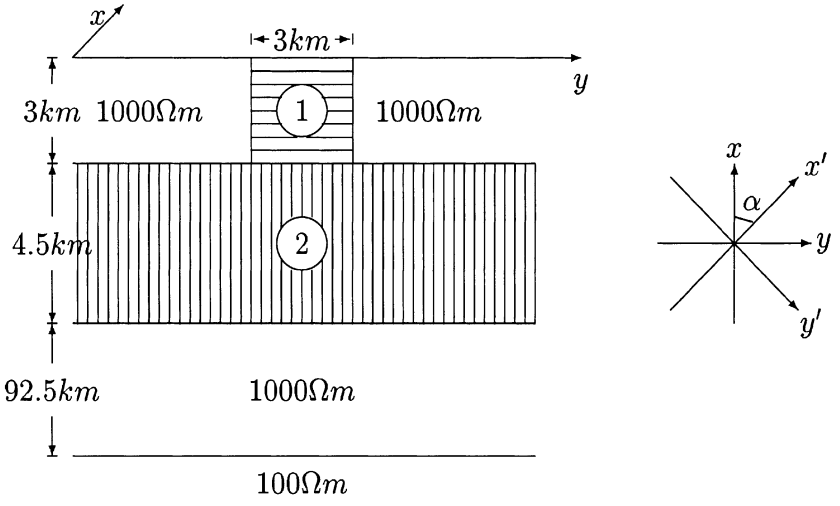

$$MEDIUM1: \quad \rho_{x'} = 30, \rho_{y'} = 100, \rho_{z'} = 30, \alpha = 30^0$$

$$MEDIUM2: \quad \rho_{x'} = 10, \rho_{y'} = 100, \rho_{z'} = 10, \alpha = 120^0$$

Figure 5. Test model for comparison of FD and FE solutions, consisting of an outcropping anisotropic block underlain by an anisotropic layer.

$|y| \to \infty$. From

$$E_{1x} = Z_{xx}H_{1x} + Z_{xy}H_{1y}, \qquad E_{1y} = Z_{yx}H_{1x} + Z_{yy}H_{1y}, \qquad (34)$$

$$E_{2x} = Z_{xx}H_{2x} + Z_{xy}H_{2y}, \qquad E_{2y} = Z_{yx}H_{2x} + Z_{yy}H_{2y}, \qquad (35)$$

we obtain the impedance tensor elements

$$Z_{xx} = (E_{1x}H_{2y} - E_{2x}H_{1y})/\det, \quad Z_{xy} = (E_{2x}H_{1x} - E_{1x}H_{2x})/\det$$

$$Z_{yx} = (E_{1y}H_{2y} - E_{2y}H_{1y})/\det, \quad Z_{yy} = (E_{2y}H_{1x} - E_{1y}H_{2x})/\det$$

$$\det = H_{1x}H_{2y} - H_{2x}H_{1y},$$

and the apparent resistivities and impedance phases

$$\rho_{ij} = \frac{1}{\omega\mu_0}|Z_{ij}|^2,$$

$$\phi_{ij} = \tan^{-1}\frac{\mathrm{Im}(Z_{ij})}{\mathrm{Re}(Z_{ij})}, \quad i, j = x, y.$$

5 NUMERICAL TEST

In order to test the adaptation of the FE method in the case of electric anisotropy, our computed results for two test models are compared with those obtained using the finite-difference

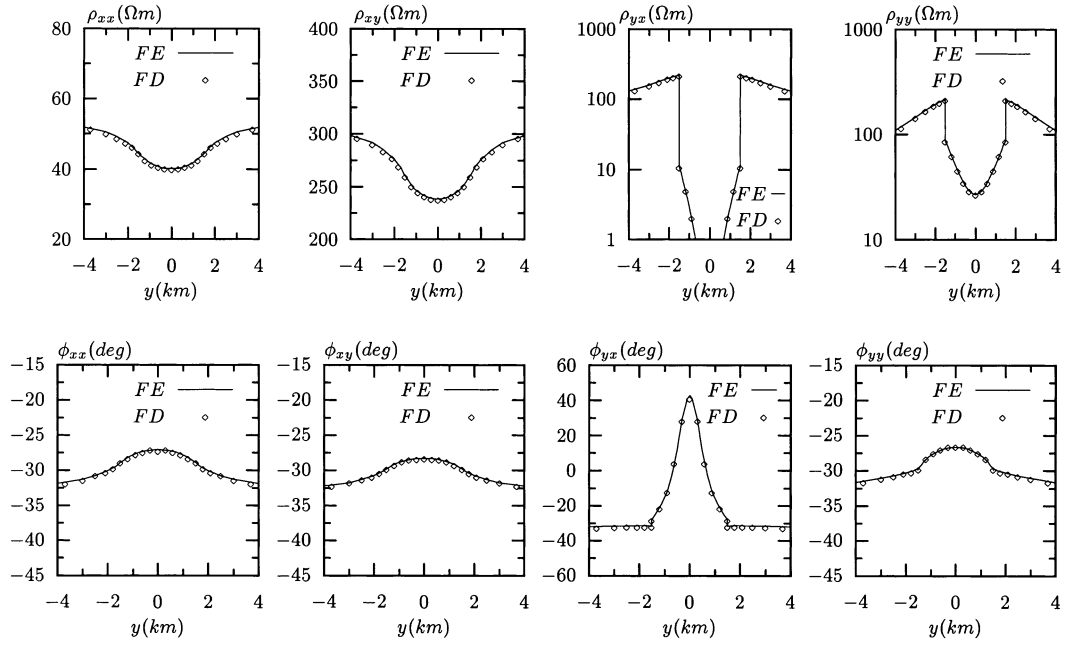

Figure 6. Apparent resistivities (top) and phases (bottom) for the model in Fig. 5. Diamonds, results of the FD algorithm (Pek & Verner 1997); solid line, results of the FE algorithm described in this paper.

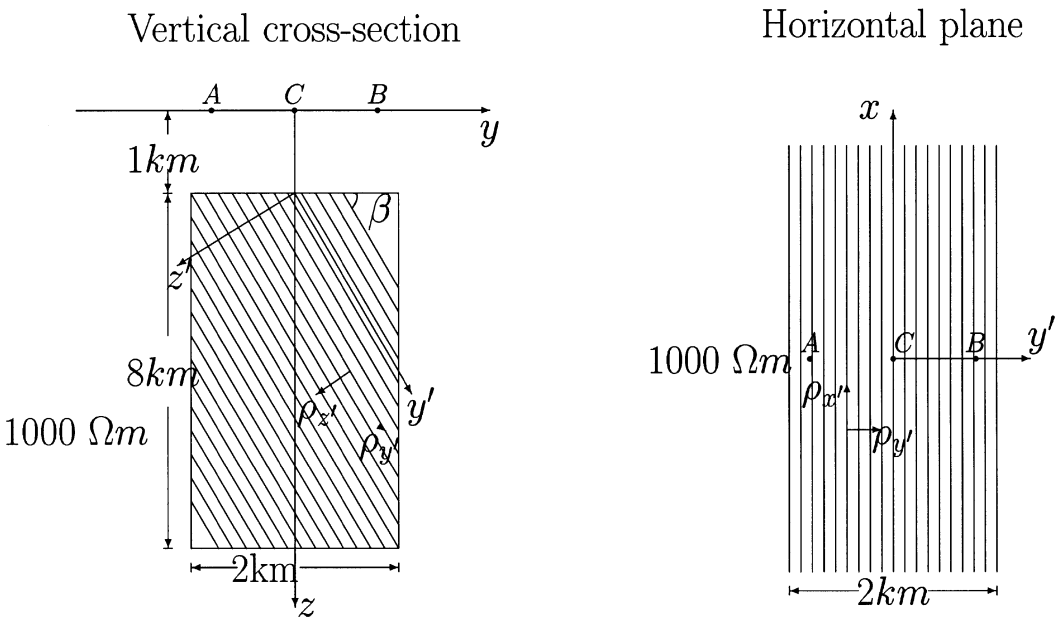

Figure 7. A 2-D slab with dipping anisotropy in an isotropic homogeneous half-space with $\rho_0 = 1000\ \Omega$ m. The conductivity tensor of the slab is given by the principal resistivities $\rho_{x'}/\rho_{y'}/\rho_{z'} = 500/10/500\ \Omega$ m for varying dip angles β.

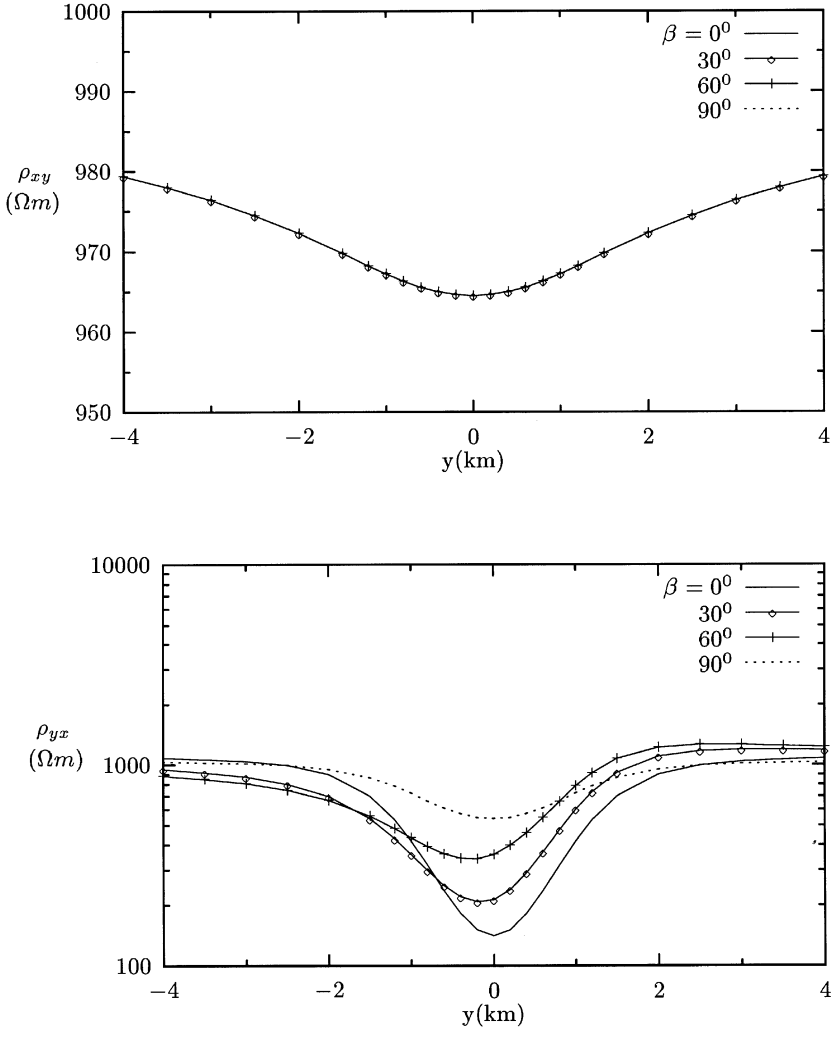

Figure 8. Apparent resistivities for various dip angles β at $T = 10$ s from Fig. 7.

method. Fig. 3 shows the first test model that was originally presented by Reddy & Rankin (1975). We computed the MT response of this model for a period of 10 s and compared it with that of the FD calculations by Pek & Verner (1997). The results are displayed in Fig. 4, and show very good agreement between the FE and FD solutions.

Fig. 5 shows the second test model presented by Pek & Verner (1997). A horizontally anisotropic layer underlies an outcropping horizontally anisotropic 2-D block. The anisotropy strikes of the two structures involved are perpendicular to each other and not parallel to the structural strike of the 2-D model. The model was chosen to demonstrate serious distortions of the MT data, which can be caused by a complicated anisotropic situation. In Fig. 6, the computed FE results for a period of 30 s are compared with those of Pek & Verner (1997). The average error in apparent resistivities is less than 0.5 per cent and the discrepancies in phases are not more than 1°.

6 EFFECTS OF ANISOTROPY

It has been noted that laterally non-uniform isotropic earth models are insufficient to account for MT tensor impedance, in particular where strong impedance anisotropies persist more or less unchanged over extended areas. This is best studied at long periods, preferably in the period range of daily variations, where the separation of ρ_a-max and ρ_a-min curves may reach two orders of magnitude or more. Near Göttingen, ρ_a-max estimated for daily variations are between 100 and 1000 Ω m, with ρ_a-min values well below 10 Ω m (Schmucker 1998). In areas with crystalline rock at the surface, similar observations have been made at much shorter periods, to which our model calculations apply. Accordingly, we have used model resistivities in the principal directions of 100–500 Ω m for x', 10 Ω m for y' and 100–500 Ω m for z'.

In this section, a simple anisotropic slab model, embedded into an isotropic homogeneous half-space with $\rho_0 = 1000$ Ω m, is used to demonstrate the effect of horizontal, vertical and dipping anisotropy upon the magnetotelluric response. All calculations are made at a period of $T = 10$ s, unless stated otherwise. For a period of 10 s the skin-depths are 50 km for the half-space and 5 km for 10 Ω m in the principal y'-direction. In particular, the dimensions of the 8 km × 2 km slab with a lower boundary at 9 km are much smaller than the half-space skin depth.

6.1 Dipping anisotropy

Fig. 7 shows how the principal axes are orientated with respect to the rectangular cross-section of the slab. The principal resistivities of the anisotropic slab are $\rho_{x'}/\rho_{y'}/\rho_{z'} = 500/10/500$, in Ω m, respectively. Fig. 8 shows the apparent resistivities for various dip angles β at a period of 10 s. This figure indicates that:

(1) the apparent resistivity ρ_{xy} is independent of the dip angle β, as the magnetotelluric field depends solely on $\rho_{xx} \equiv \rho_{x'}$ in this case and is not affected by the anisotropy;

(2) the apparent resistivity ρ_{yx} is affected considerably by β. The ρ_{yx} curves are not symmetric with respect to the centre of the model—the minimum of the curves is off-centre and shifted to one side depending on the sign of the dip. This shift increases with increasing deviation of the dip from either the horizontal or vertical direction. We can explain this behaviour by looking at the distribution of the electrical fields. Fig. 9 shows the distribution of the electrical field in the yz-plane for three dip angles β (= 30°, 60°, 90°) in the polarization 1, in which the generating primary magnetic field is $\mathbf{H}_0 = (-1, 0, 0)$. The starting point of each arrow is the finite-element node. The length and the direction of the arrows reflect the magnitude and the direction of the field at that point. The figure clearly shows that the magnitude and the direction of the field change with the dip angle β within the anisotropic slab.

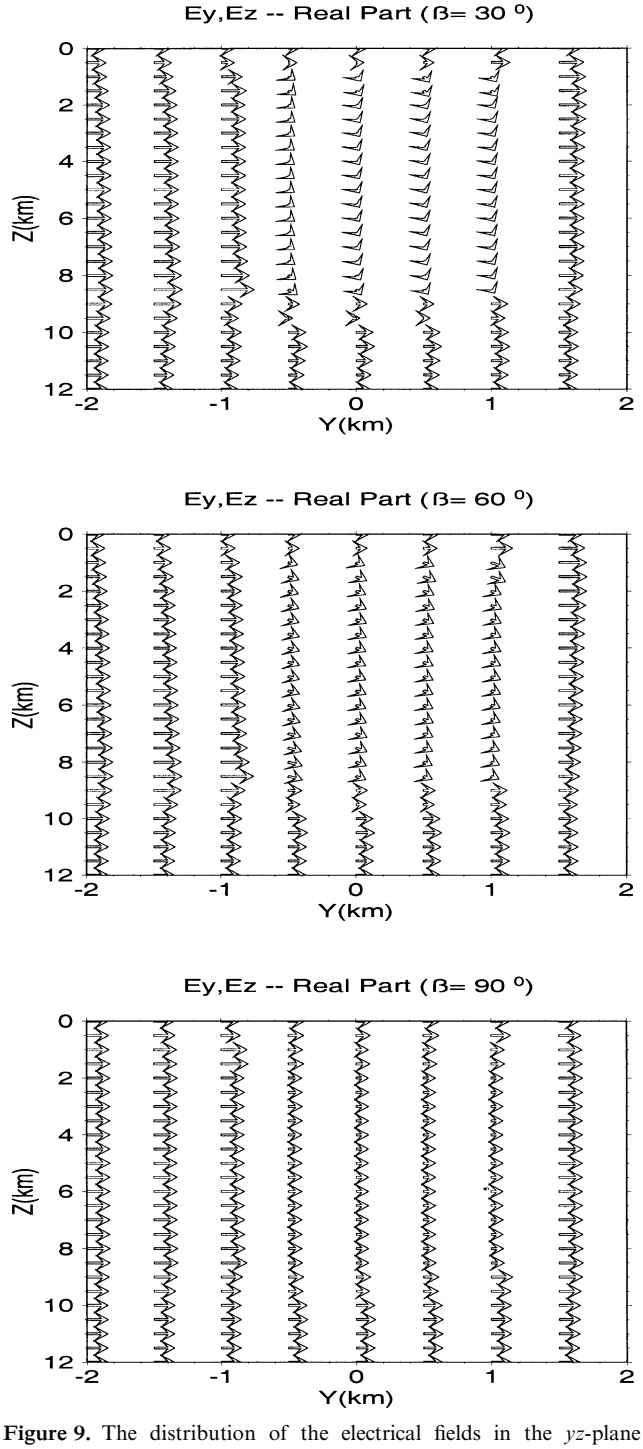

Figure 9. The distribution of the electrical fields in the yz-plane for the model in Fig. 7. The generating primary magnetic field is $\mathbf{H}_0 = (-1, 0, 0)$ and the period of the field is 10 s.

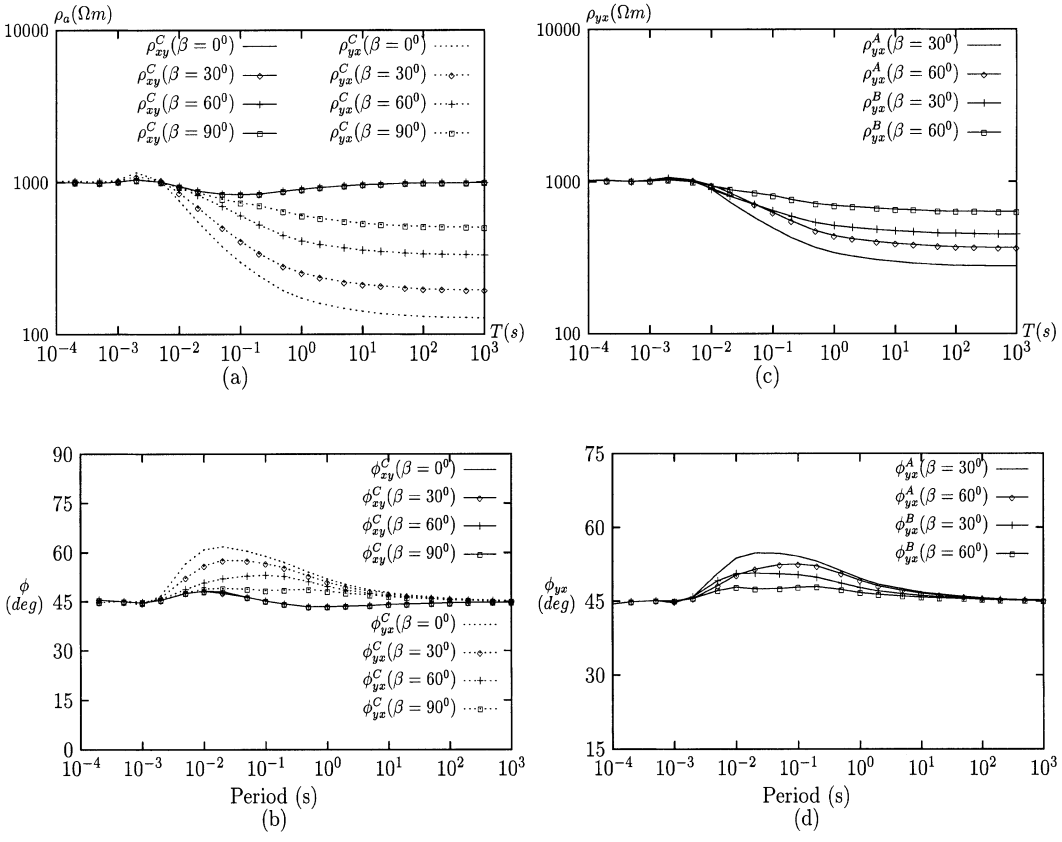

Figure 10. The apparent resistivity and phase curves at the surface points A, B and C for the model in Fig. 7.

(3) If $\beta=0$, ρ_{yx} corresponds to the apparent resistivity produced by a model with resistivities of 10 Ω m along the y direction and 500 Ω m along x and z directions. Similarly, if $\beta=90°$, ρ_{yx} corresponds to that produced by a model with vertical anisotropy, with the resistivities 500 Ω m along x and y directions and 10 Ω m along the z direction.

The apparent resistivity and phase curves for various dip angles β ($=0°$, $30°$, $60°$, $90°$) at the model centre C ($y_C=0$) are shown in Figs 10(a) and (b), respectively. From these figures one can see that the apparent resistivities at very short periods approach the true resistivity of the half-space, and the phases approach 45°. However, with increasing period ρ^C_{xy} and ρ^C_{yx} deviate significantly, ϕ^C_{xy} and ϕ^C_{yx} too, and this deviation is dependent on the dip angle β. While ρ^C_{yx} and ϕ^C_{yx} curves are distinct for different dip angles β, the ρ^C_{xy} and ϕ^C_{xy} curves coincide with each other. Moreover, the apparent resistivity ρ^C_{xy} at the very long periods converges to the value appropriate for the resistivity of the half-space, the phases ϕ^C_{xy} and ϕ^C_{yx} approach 45°, but ρ^C_{yx} is still under the influence of the anisotropic slab. The apparent resistivity ρ_{yx} and phase ϕ_{yx} at the surface points $A(y_A=-0.8$ km) and $B(y_B=0.8$ km), which are symmetric with respect to the model centre C, are shown in Figs 10(c) and (d), respectively. From these figures it can be seen that the apparent resistivity and phase curves at A, ρ^A_{yx} and ϕ^A_{yx} are different from

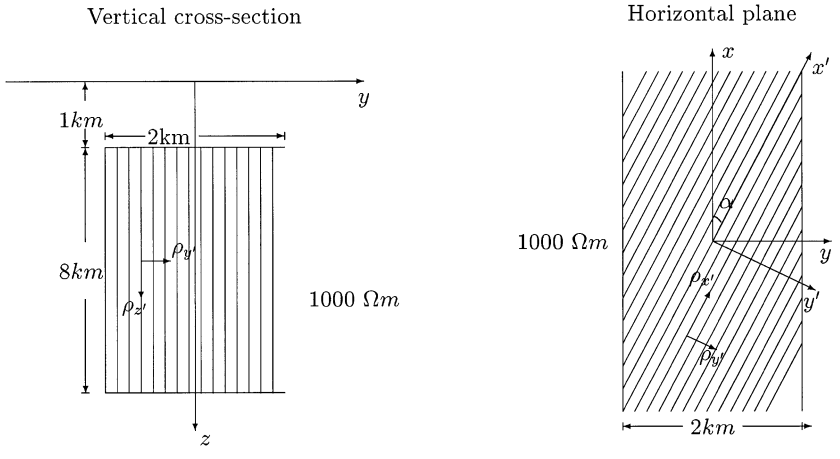

Figure 11. A 2-D slab with horizontal anisotropy in an isotropic homogeneous half-space with $\rho_0=1000$ Ω m. The conductivity tensor of the slab is given by the principal resistivities $\rho_{x'}/\rho_{y'}/\rho_{z'}=100/10/100$ Ω m for varying anisotropic strike angles α.

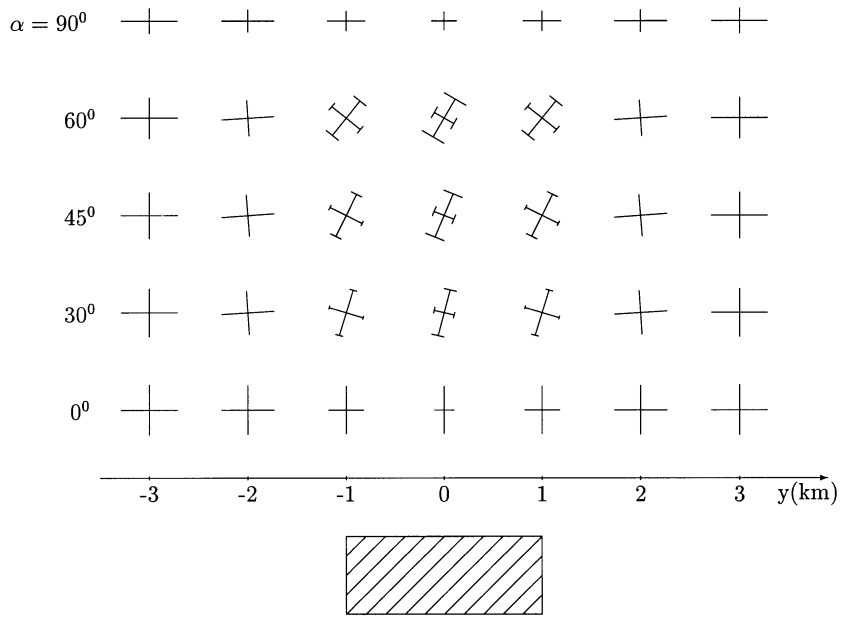

Figure 12. MT principal axes for various strike angles α. Cross, absolute values of the off-diagonal MT tensor elements $Z_{x''y''}$, $Z_{y''x''}$; crossbars, absolute values of the diagonal MT tensor elements $Z_{x''x''}$, $Z_{y''y''}$ with reference to Swift-rotated coordinates (x'', y'').

those at *B*. However, they coincide with each other, when $\beta = 0^\circ$ and 90°. It is easily seen that the apparent resistivity ρ_{xy} and phase ϕ_{xy} at *A* are identical with those at *B*.

6.2 Horizontal anisotropy

Fig. 11 shows the orientation of the principal axes, which are now tilted in the horizontal plane by an angle α. The principal resistivities of the anisotropic inhomogeneity are $\rho_{x'}/\rho_{y'}/\rho_{z'} =$ 100/10/100, respectively, in Ω m. According to the technique of Siemon (1997), the magnitudes of the rotated off-diagonal impedance elements, $|Z_{x''y''}|$ and $|Z_{y''x''}|$, are plotted along the coordinate axes, rotated into the Swift principal direction, and the diagonal impedances, $|Z_{x''x''}|$ and $|Z_{y''y''}|$, attached to them as cross-bars. Fig. 12 shows the magnetotelluric impedances in Siemon's representation along a surface profile for various anisotropy strike angles α at a period of 10 s. From Fig. 12 we can conclude that:

(1) immediately above the anisotropic block, the minimum and maximum axes indicate the direction of the high and low conductivity, respectively;

(2) significant diagonal elements of the impedance tensor, $|Z_{x''x''}|$ and $|Z_{y''y''}|$, exist (except for $\alpha = 0^\circ$ and 90°), and increase

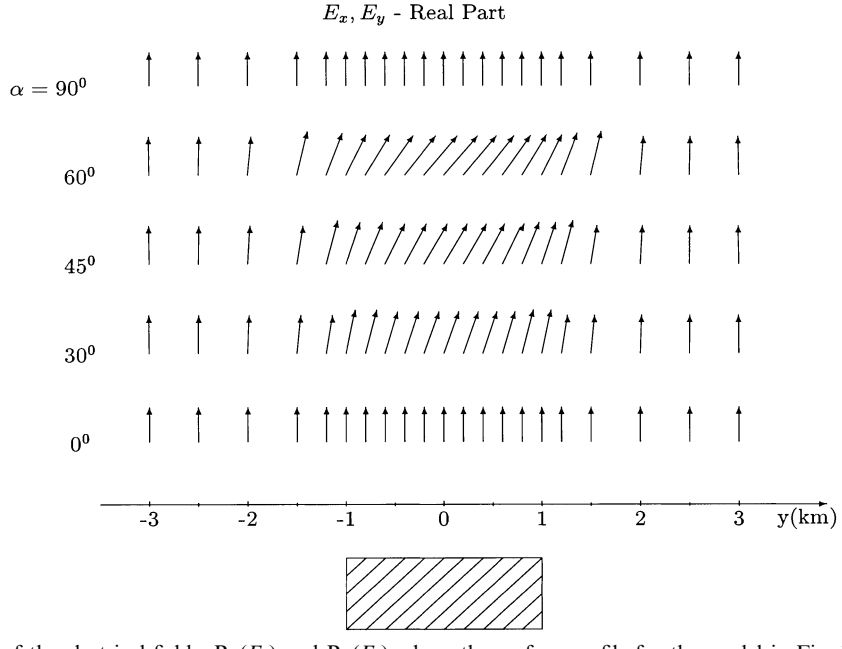

Figure 13. The real parts of the electrical fields, Re(E_x) and Re(E_y), along the surface profile for the model in Fig. 11. The generating primary magnetic field is $\mathbf{H}_0 = (0, 1, 0)$ and the period of the field is 10 s.

with the deviation of the anisotropy strike α from the structural strike of the model;

(3) far from the inhomogeneity, where the anomalous field fades out, the off-diagonal elements become equal, $|Z_{x''y''}| = |Z_{y''x''}|$, and the diagonal elements disappear: $|Z_{x''x''}| = |Z_{y''y''}| \to 0$ for $|y| \to \infty$. When passing through the edge of the anisotropic block towards the homogeneous half-space, a certain reduction of the impedances takes place within a transition zone where the above directional pattern can be severely distorted, especially if large anisotropies and shallow anomalous conductors are involved.

Fig. 13 shows the real parts of the electrical fields, $\mathrm{Re}(E_x)$ and $\mathrm{Re}(E_y)$, along the surface profile for the various strike angles $\alpha(=0^\circ, 30^\circ, 45^\circ, 60^\circ, 90^\circ)$ in polarization 2, in which the generating primary magnetic field is $\mathbf{H}_0=(0, 1, 0)$. It can be seen from this figure that the magnitude and the direction of the field change with the strike angle α within the anisotropic slab; the y-component of the electrical field, $\mathrm{Re}(E_y)$ exists except that $\alpha=0^\circ$ and 90°, and becomes greater when the strike angle α is in between these values.

6.3 A tilted slab model

Fig. 14 shows a 2-D model as in Fig. 7 for the special case of $\beta=90^\circ$, but the slab is tilted by 45°, simulating a direction-dependent conductivity in a shear or subduction zone. Owing to shearing, it could be expected that the slab has different conductivities in the direction of shearing and perpendicular to it. If no such difference exists and assuming that the slab as a whole is a better conductor than the surrounding layer, a non-symmetric central minimum in ρ_a is observed for a primary field in the strike direction. If the parallel resistivity is 10 times greater than resistive surrounding rocks, the asymmetry is preserved, but with a barely visible minimum above the slab. If the slab is a much better conductor in the direction of shearing, then the minimum in ρ_{yx} is more pronounced, as is to be expected (Fig. 15a). With respect to the splitting of ρ_a-curve, Fig. 15(b) shows that it begins well below 1 s and that it merges into a quasi-static offset for longer periods.

7 CONCLUSIONS

We have presented an algorithm for the numerical modelling of magnetotelluric fields in anisotropic 2-D structures. The main features of our numerical scheme are as follows.

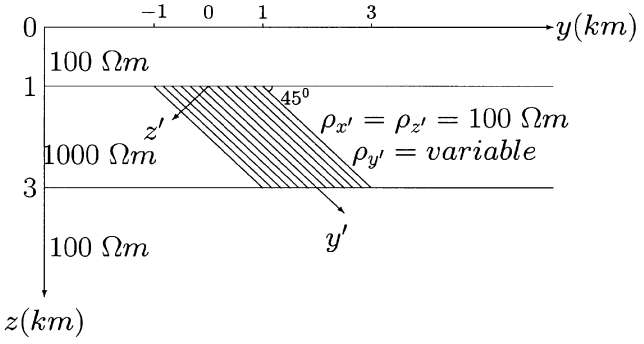

Figure 14. A 2-D model as in Fig. 7 for the special case of $\beta=90^\circ$, but the slab is tilted by 45°, simulating a shear or subduction zone with different resistivities parallel and perpendicular to the slab boundaries.

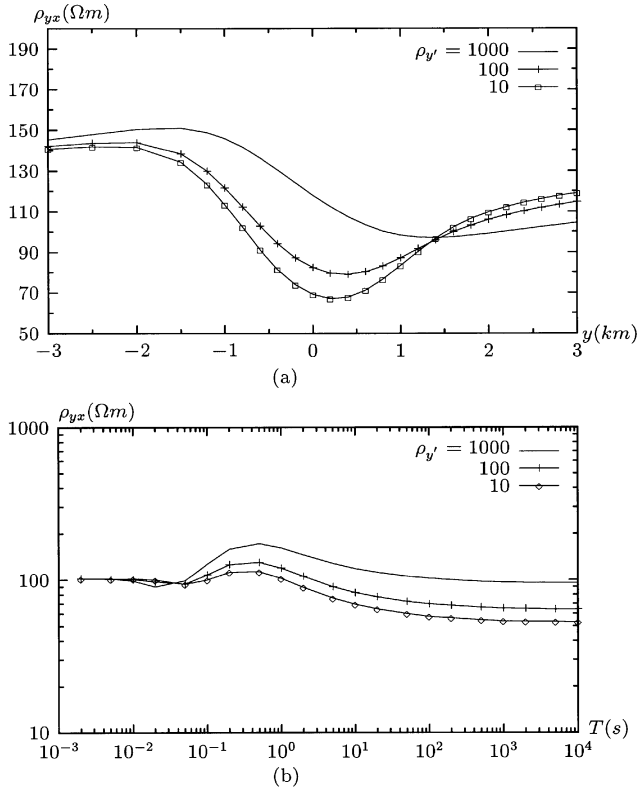

Figure 15. Apparent resistivities ρ_{yx} on a profile across the slab for $T=10$ s (a) and apparent resistivity curves at the site $y=0$ (b) for the tilted slab model of Fig. 14. Resistivity $\rho_{y'}$, parallel to slab boundary, either equal to the highly resistive host rocks, or equal to $\rho_{z'}$ perpendicular to slab boundary (isotropic case), or 10 times less than $\rho_{z'}$. Apparent resistivities ρ_{xy} curves for $\rho_{y'}$ between 10 and 1000 Ω m follow the ρ_{yx} curve closely for $\rho_{y'}=1000$ Ω m.

(1) The conductivity tensor of each anisotropic block is represented by a symmetric 3×3 matrix, thus allowing us an arbitrary anisotropy to be considered within the medium, including the special cases of the horizontal, vertical and dipping anisotropy.

(2) The numerical treatment of the problem involved is based upon the finite-element method, which is well suited to sloping model boundaries and topography, as exemplified in Fig. 14.

(3) Assuming a very small, but positive air conductivity, the air layer can be integrated into the conductive model. The equations for both modes can then be approximated homogeneously over the entire model area, which makes the approximation process much simpler than distinguishing the air-and-earth and earth-only variables as done by Pek & Verner (1997), with the air conductivity set exactly to zero. With fast iterative techniques used to solve the system of FE linear equations, the additional H_x-variables within the air layer do not present an excessive problem. The numerical experiments performed show that the solution for the field components is stable and practically unaffected within broad limits of the air conductivity chosen, specifically from 10^{-12} Sm^{-1}, which is small enough for rock conductivities and well below the extremely low conductivity of air above the earth.

(4) A modified conjugate gradient technique is used to solve the equation system eq. (33), with a complex and symmetric matrix. We found that a simple diagonal scaling (Jacobi scaling) is a sufficient preconditioner in our case.

(5) The strike-perpendicular field components E_y and H_y are computed numerically using the spline interpolation.

ACKNOWLEDGMENTS

The author would like to express his thanks to Dr U. Schmucker and Dr J. Pek for many stimulating discussions and for improving the manuscript. Dr J. Pek also provided the 1-D forward program for MT anisotropic structure and the FD results for the two test models. Thanks are also due to Martyn Unsworth, Chester Weiss and another anonymous referee for their constructive comments. The author wishes to thank the Deutscher Akademischer Austauschdienst (German Academic Exchange Service) for offering a PhD scholarship. This work was conducted at the Geophysical Institute, University of Göttingen.

REFERENCES

Eisel, M. & Haak, V., 1999. Macro-anisotropy of the electrical conductivity of the crust: a magneto-telluric study from the German Continental Deep Drilling site (KTB), *Geophys. J. Int.,* **136,** 109–122.

Hestens, M.R. & Stiefel, E., 1952. Method of conjugate gradients for solving linear systems, *J. Res. Nat. Bur. Stand.,* **49,** 409–436.

Jacobs, D.A.H., 1981. The exploitation of sparsity by iterative methods, in *Sparse Matrics and their Uses,* pp. 191–222, ed. Duff, I.S., Springer, Berlin.

Kellett, R.L., Mareschal, M. & Kurtz, R.D., 1992. A model of lower crustal electrical anisotropiy for the Pontiac Subprovince of the Canadian Shield, *Geophys. J. Int.,* **111,** 141–150.

Li, Y., 2000. Finite element modeling of electromagnetic fields in two- and three-dimensional anisotropic conductivity structures, *PhD thesis,* University of Göttingen.

Mareschal, M., Kellett, R.L., Kurtz, R.D., Ludden, J.N., Ji, S., & Bailey, R.C., 1995. Archaean cratonic roots, mantle shear zones and deep electrical anisotropy, *Nature,* **375,** 6527, 134–137.

O'Brien, D.P. & Morrison, H.F., 1967. Electromagnetic fields in an *N* layer anisotropic half space, *Geophysics,* **32,** 668–677.

Osella, A.M. & Martinelli, P., 1993. Magnetotelluric response of anisotropic 2-D structures, *Geophys. J. Int.,* **115,** 819–828.

Pek, J. & Verner, T., 1997. Finite-difference modelling of magneto-telluric fields in two-dimensional anisotropic media, *Geophys. J. Int.,* **128,** 505–521.

Rasmussen, T.M., 1988. Magnetotellurics in southwestern Sweden; evidence for electrical anisotropy in the lower crust?, *J. geophys. Res.,* **93,** 7897–7907.

Reddy, I.K. & Rankin, D., 1975. Magnetotelluric response of laterally inhomogeneous and anisotropic media, *Geophysics,* **40,** 1035–1045.

Schwarz, H.R., 1991. *Methode der finiten Elemente: eine Einführung under besonderer Berücksichtigung der Rechenpraxis,* Teubner, Stuttgart.

Schmucker, U., 1994. 2-D Modellrechnungen zur Induktion in inhomogenen dünnen Schichten über anisotropen geschichteten Halbräumen, in *Protokoll Kolloquium, 'Elektromagnetische Tiefenforschung',* Höchst in Odenwald, pp. 3–26, eds Bahr, K. and Junge, A., DGG.

Schmucker, U., 1998. Magnetotellurische Übertragungsfunktionen für den Tagesgang and das langperiodisches Kontinuum an zwei Stationen in der Umgebung von Göttingen. in *Protokoll Kolloquium, 'Elektromagnetische Tiefenforschung',* Neustadt an der Weinstrasse, pp. 374–397, eds Junge, A. and Bahr, K., DGG.

Siemon, B., 1997. An interpretation technique for superimposed induction anomalies, *Geophys. J. Int.,* **130,** 73–88.

Weidelt, P., 1996. Elektromagnetische Induktion in dreidimensional anisotropen Leitern, in *Protokoll Kolloquium 'Elektromagnetische Tiefenforschung',* Burg Ludwigstein, pp. 60–73, eds Bahr, K. and Junge, A., DGG.

APPENDIX A: DERIVATION OF THE LINEAR EQUATION SYSTEM

The first integral of eq. (25) over an element e is

$$\frac{1}{i\omega\mu_0}\int_e \nabla E_x\cdot\nabla\delta E_x\,d\Omega=\delta\mathbf{E}_{xe}^{\mathrm{T}}\mathbf{K}_{1e}\,\mathbf{E}_{xe}\,, \tag{A1}$$

where $\mathbf{E}_{xe}=(E_1,\,E_2,\,E_3)^{\mathrm{T}}$, $\delta\mathbf{E}_{xe}^{\mathrm{T}}=(\delta E_1,\,\delta E_2,\,\delta E_3)$ and $\mathbf{K}_{1e}$ is a 3×3 symmetric matrix with the elements

$$\mathbf{K}_{1e}=\frac{1}{i\omega\mu_0}\,\frac{1}{4\Delta}\begin{pmatrix} a_1^2+b_1^2 & & sym.\\ a_1a_2+b_1b_2 & a_2^2+b_2^2 & \\ a_1a_3+b_1b_3 & a_2a_3+b_2b_3 & a_3^2+b_3^3\end{pmatrix}.$$

The second integral of eq. (25) over the element e is

$$-\int_e C\,E_x\,\delta E_x\,d\Omega=\delta\mathbf{E}_{xe}^{\mathrm{T}}\mathbf{K}_{2e}\,\mathbf{E}_{xe}\,, \tag{A2}$$

where

$$\mathbf{K}_{2e}=-\frac{C\Delta}{12}\begin{pmatrix}2 & & sym.\\ 1 & 2 & \\ 1 & 1 & 2\end{pmatrix}.$$

The third integral of eq. (25) over the element e is

$$\int_e\left(-A\,\frac{\partial H_x}{\partial y}+B\,\frac{\partial H_x}{\partial z}\right)\delta E_x\,d\Omega=\delta\mathbf{E}_{xe}^{\mathrm{T}}\,\mathbf{K}_{3e}\mathbf{H}_{xe} \tag{A3}$$

where $\mathbf{H}_{xe}=(H_1,\,H_2,\,H_3)^{\mathrm{T}}$ and $\mathbf{K}_{3e}$ is a non-symmetric matrix

$$\mathbf{K}_{3e}=\frac{1}{6}\begin{pmatrix}-Aa_1+Bb_1 & -Aa_2+Bb_2 & -Aa_3+Bb_3\\ -Aa_1+Bb_1 & -Aa_2+Bb_2 & -Aa_3+Bb_3\\ -Aa_1+Bb_1 & -Aa_2+Bb_2 & -Aa_3+Bb_3\end{pmatrix}.$$

Before summing up the integrals over all the elements, the column vectors of individual element $\mathbf{E}_{xe}$, $\mathbf{H}_{xe}$ and $\delta\mathbf{E}_{xe}$, each with three components, are grouped into global vectors $\mathbf{E}_x=(E_1,\ldots,E_{n_d})^{\mathrm{T}}$, $\mathbf{H}_x=(H_1,\ldots,H_{n_d})^{\mathrm{T}}$ and $\delta\mathbf{E}_x=(\delta E_1,\ldots,\delta E_{n_d})^{\mathrm{T}}$, where n_d is the total number of nodal points over the entire model area Ω. The element matrices $\mathbf{K}_{1e}$, $\mathbf{K}_{2e}$ and $\mathbf{K}_{3e}$, each of size of 3×3, are expanded to $\overline{\mathbf{K}}_{1e}$, $\overline{\mathbf{K}}_{2e}$ and $\overline{\mathbf{K}}_{3e}$ with n_d rows and n_d columns, respectively. This is done by adding rows and columns of zeros to the element matrices. The sum of the integrals (25) over all elements gives

$$\delta\mathbf{E}_x^{\mathrm{T}}\left(\sum_{e=1}^{n_e}\overline{\mathbf{K}_{1e}}+\sum_{e=1}^{n_e}\overline{\mathbf{K}_{2e}}\right)\mathbf{E}_x+\delta\mathbf{E}_x^{\mathrm{T}}\sum_{e=1}^{n_e}\overline{\mathbf{K}_{3e}}\,\mathbf{H}_x=0\,, \tag{A4}$$

or

$$\delta\mathbf{E}_x^{\mathrm{T}}\,\mathbf{K}_{11}\,\mathbf{E}_x+\delta\mathbf{E}_x^{\mathrm{T}}\,\mathbf{K}_{12}\,\mathbf{H}_x=0\,, \tag{A5}$$

with

$$\mathbf{K}_{11}=\sum_{e=1}^{n_e}\overline{\mathbf{K}}_{1e}+\sum_{e=1}^{n_e}\overline{\mathbf{K}}_{2e}\,,\quad \mathbf{K}_{12}=\sum_{e=1}^{n_e}\overline{\mathbf{K}}_{3e}\,.$$

The matrix $\mathbf{K}_{11}$ is a symmetric square matrix of order n_d, $\mathbf{K}_{12}$ a non-symmetric square matrix of the order n_d.

Considering that $\delta \mathbf{E}_x$ is arbitrary, we arrive at

$$\mathbf{K}_{11}\,\mathbf{E}_x + \mathbf{K}_{12}\,\mathbf{H}_x = 0\,, \tag{A6}$$

which is a system of n_d linear equations with $2n_d$ unknowns $E_1, \ldots, E_{n_d}$, and $H_1, \ldots, H_{n_d}$.

To find the solution for $\mathbf{E}_x$ and $\mathbf{H}_x$, we must further derive another linear equation system for the above variables using eq. (26). The first integral of eq. (26) over an element e is

$$\int_e \nabla \delta H_x \cdot \underline{\tau}\, \nabla \delta H_x \, d\Omega = \delta \mathbf{H}_{xe}^{\mathrm{T}}\, \mathbf{K}_{4e}\, \mathbf{H}_{xe}\,, \tag{A7}$$

where $\mathbf{H}_{xe} = (H_1, H_2, H_3)^{\mathrm{T}}$ and $\delta H_{xe} = (\delta H_1, \delta H_2, \delta H_3)^{\mathrm{T}}$. $\mathbf{K}_{4e}$ is a symmetric 3×3 matrix,

$$\mathbf{K}_{4e} = \frac{1}{4\Delta} \begin{pmatrix} \alpha_1 a_1 + \beta_1 b_1 & \alpha_1 a_2 + \beta_1 b_2 & \alpha_1 a_3 + \beta_1 b_3 \\ \alpha_1 a_2 + \beta_1 b_2 & \alpha_2 a_2 + \beta_2 b_2 & \alpha_2 a_3 + \beta_2 b_3 \\ \alpha_1 a_3 + \beta_1 b_3 & \alpha_2 a_3 + \beta_2 b_3 & \alpha_3 a_3 + \beta_3 b_3 \end{pmatrix},$$

with

$$\alpha_1 = \tau_{11} a_1 + \tau_{21} b_1\,, \quad \alpha_2 = \tau_{11} a_2 + \tau_{21} b_2\,, \quad \alpha_3 = \tau_{11} a_3 + \tau_{21} b_3\,,$$

$$\beta_1 = \tau_{12} a_1 + \tau_{22} b_1\,, \quad \beta_2 = \tau_{12} a_2 + \tau_{22} b_2\,, \quad \beta_3 = \tau_{12} a_3 + \tau_{22} b_3\,.$$

The second integral of eq. (26) over the element e is

$$-\int_e i\omega\mu_0 H_x \, \delta H_x \, d\Omega = \delta \mathbf{H}_{xe}^{\mathrm{T}}\, \mathbf{K}_{5e}\, \mathbf{H}_{xe}\,, \tag{A8}$$

with

$$\mathbf{K}_{5e} = -\frac{\mathrm{i}\omega\mu_0\Delta}{12} \begin{pmatrix} 2 & & sym. \\ 1 & 2 & \\ 1 & 1 & 2 \end{pmatrix}.$$

The third integral of eq. (26) over the element e is, again with the use of eq. (16),

$$\int_e \mathbf{p} \cdot \nabla \delta H_x d\Omega = \delta \mathbf{H}_{xe}^{\mathrm{T}} \mathbf{K}_{6e} \mathbf{E}_{xe}\,, \tag{A9}$$

with

$$\mathbf{K}_{6e} = \frac{1}{6} \begin{pmatrix} -Aa_1 + Bb_1 & -Aa_1 + Bb_1 & -Aa_1 + Bb_1 \\ -Aa_2 + Bb_2 & -Aa_2 + Bb_2 & -Aa_2 + Bb_2 \\ -Aa_3 + Bb_3 & -Aa_3 + Bb_3 & -Aa_3 + Bb_3 \end{pmatrix}.$$

Comparing the latter matrix with $\mathbf{K}_{3e}$, we can see that $\mathbf{K}_{3e} = \mathbf{K}_{6e}^{\mathrm{T}}$.

Consistently with the previously used arrangement of the mesh nodes, the single-element vectors $\mathbf{E}_{xe}$, $\mathbf{H}_{xe}$ and δH_{xe} are again grouped into $\mathbf{E}_x = (E_1, \ldots, E_{n_d})^{\mathrm{T}}$, $\mathbf{H}_x = (H_1, \ldots, H_{n_d})^{\mathrm{T}}$ and $\delta H_x = (\delta H_1, \ldots, \delta H_{n_d})^{\mathrm{T}}$, respectively, and the matrices $\mathbf{K}_{4e}$, $\mathbf{K}_{5e}$ and $\mathbf{K}_{6e}$ are expanded to $\overline{\mathbf{K}}_{4e}$, $\overline{\mathbf{K}}_{5e}$ and $\overline{\mathbf{K}}_{6e}$, respectively, all of the order n_d. The sum of the integrals in eq. (26) over all the elements finally results in

$$\delta \mathbf{H}_x^{\mathrm{T}} \left(\sum_{e=1}^{n_e} \overline{\mathbf{K}}_{4e} + \sum_{e=1}^{n_e} \overline{\mathbf{K}}_{5e} \right) \mathbf{H}_x + \delta \mathbf{H}_x^{\mathrm{T}} \sum_{e=1}^{n_e} \overline{\mathbf{K}}_{6e}\, \mathbf{E}_x = 0\,, \tag{A10}$$

or

$$\delta \mathbf{H}_x^{\mathrm{T}}\, \mathbf{K}_{22}\, \mathbf{H}_x + \delta \mathbf{H}_x^{\mathrm{T}} \mathbf{K}_{21}\, \mathbf{E}_x = 0\,, \tag{A11}$$

with

$$\mathbf{K}_{21} = \sum_{e=1}^{n_e} \overline{\mathbf{K}}_{6e}, \quad \mathbf{K}_{22} = \sum_{e=1}^{n_e} \overline{\mathbf{K}}_{4e} + \sum_{e=1}^{n_e} \overline{\mathbf{K}}_{5e}.$$

Since $\delta \mathbf{H}_x$ is arbitrary, we finally obtain a linear equation system

$$\mathbf{K}_{21}\, \mathbf{E}_x + \mathbf{K}_{22}\, \mathbf{H}_x = 0\,. \tag{A12}$$